Low dose Taxol causes mitochondrial dysfunction in actively respiring cancer cells

Received for publication, September 13, 2024, and in revised form, March 3, 2025 Published, Papers in Press, March 25, 2025,
https://doi.org/10.1016/j.jbc.2025.108450

Rozhin Penjweini[1,‡], Katie A. Link[1,‡], Shureed Qazi[1], Nikhil Mattu[1], Adam Zuchowski[1], Alexandra Vasta[1], Dan L. Sackett[2,*], and Jay R. Knutson[1,*]

From the [1]Laboratory of Advanced Microscopy and Biophotonics, National Heart, Lung, and Blood Institute (NHLBI), and [2]Cytoskeletal Dynamics Group, Division of Basic and Translational Biophysics, Eunice Kennedy Shriver National Institute of Child Health and Human Development, NIH, Bethesda, Maryland, USA

Reviewed by members of the JBC Editorial Board. Edited by Karen Fleming

Mitochondrial oxygen consumption, dynamics, and morphology play roles in the occurrence, development, and drug resistance of cancer; thus, they are main targets for many anticancer drugs. Increased mitochondrial oxygen consumption and impaired oxygen delivery creates hypoxia, which influences the balance of metabolic cofactors for biogenesis, disease progression, and response to therapeutics. We therefore investigated the effects of Taxol, a well-known anticancer drug, on mitochondrial respiration (principally *via* a measure of oxidative phosphorylation *versus* glycolysis), morphology, and dynamics. The concomitant effects of Taxol on mitochondrial ATP and reactive oxygen species production, mitochondrial membrane potential, radical-induced formation of carbonyl groups, mitochondrial release of cytochrome *c*, as well as cell cycle were investigated. Cells used in this study include the following: A549 (non-small-cell lung epithelial cancer cell line), A549-ρ^0 (mitochondrial DNA-depleted derivative of A549), and BEAS-2B (a noncancer cell line derived from normal bronchial epithelium), as well as PC3 (prostate cancer) and HepG2 (hepatocellular carcinoma); these cell lines are known to have disparate metabolic profiles. Using a multitude of fluorescence-based measurements, we show that Taxol, even at a low dose, still adversely affects mitochondria of actively respiring (aerobic) cancer cells. We find an increase in mitochondrial ROS and cytochrome *c* release, suppression of ATP production and oxidative phosphorylation, fragmentation of the mitochondrial network, and disruption of mitochondria-microtubule linkage. We find these changes in oxidative, but not glycolytic, cancer cells. Noncancer cells, which are oxidative, do not show these changes.

Taxol (generic name: paclitaxel) is an antineoplastic drug approved by the Food and Drug Administration and is one of the most frequently used chemotherapies to treat human malignancies, including lung and breast cancers (1). Microtubules are the proximal cellular target of Taxol (2), but the postbinding mechanisms of action that explain Taxol's clinical efficacy are constantly debated in the scientific community (1). Some studies propose chromosome mis-segregation-driven cell death (3) or the disruption of the microtubule-dependent transport of cellular cargo as the main mechanisms to account for the therapeutic efficacy of Taxol (4). More recently, a nonmitotic mechanism of action has been suggested wherein Taxol-induced rigid microtubules cause breakage in malleable cancer nuclei resulting in multiple micronuclei (5). These micronuclei have defective membrane structures with a proclivity to rupture, resulting in a release of chromatin material causing compromised cellular structure and eventual cell death.

There have been extensive studies with varying Taxol concentration/exposure time *versus* cell viability and damage. At moderately high doses (*e.g.* 0.1–1 μM for ≥ 24 h), Taxol induces an increase in the fraction of cellular tubulin that is polymerized, as well as bundling of microtubules, causing loss of net positional polarization of microtubule arrays (6). For some time, this was thought to be the proximal cause of Taxol-induced dysfunction (such as mitotic arrest and blockage of intracellular directional transport). It was discovered, however, that at lower doses of Taxol, mitotic block was induced without an increase in the polymerized fraction of tubulin and without causing microtubule bundling, due to inhibition of microtubule assembly dynamics (7). Further studies showed, in multiple cell types, that at or below 10 to 30 nM Taxol for ≤ 24 h exposure, microtubule dynamics are altered without inducing accumulation of additional polymer (8).

Since microtubules are responsible for transporting mitochondria, with network mobility essential for balanced distribution (9), disruptions in the microtubule network may impede mitochondrial transport and further disrupt mitochondrial morphology and distribution within cells. Additionally, studies have alluded to altered mitochondrial biogenesis and metabolism that could be affected by microtubule targeting drugs (1). Abnormal changes to mitochondria have been indicated in the pathogenesis of cancer and other diseases (10). Thus, understanding the implications of microtubule targeting drugs such as Taxol on mitochondrial health, distribution, and function is paramount to understanding the full impact of these therapeutics.

‡ These authors contributed equally to this work.
* For correspondence: Jay R. Knutson, knutsonj@nhlbi.nih.gov; Dan L. Sackett, sackettd@mail.nih.gov.

To further understand the mechanistic effects of Taxol on cells, with direct impact on mitochondria at the forefront, we treated a variety of cancer cells with a low dose of Taxol (10 nM for 18 h). Our dose selection was based on the studies of lactate dehydrogenase (LDH) release induced by different Taxol doses (see Fig. S1, *A–D* in the Supporting Information) and many previous dose-response studies, referred to above, and which lead to a definition of 'low' doses being at or below 10 to 30 nM for ≤ 24 h (7, 11). We establish this level to study the *initial* damage to the cell brought about by the loss of microtubule dynamics induced by Taxol.

It is important to note, while it is true that this dose (10 nM, 18 h) has been shown to not induce bundling of microtubules in the cell and to not increase the fraction of tubulin polymerized into microtubules (7, 8), it is definitely still a cytotoxic dose of the drug. These studies that showed a lack of bundling or hyperpolymerization also reported that this same drug regimen altered microtubule dynamics by stabilizing microtubules against end-driven depolymerization and that this loss of dynamics led to a shift in the cell cycle, resulting in mitotic arrest. Exposure of cells for a longer time to the same low concentration of Taxol results in the arrest of growth and cell death. For example, the average GI50 (concentration resulting in 50% growth inhibition) for all the cell lines in the NCI cancer cell screen is about 13 nM for a 4-days exposure (see website link in (https://dtp.cancer.gov/dtpstandard/dwindex/index.jsp)). By using a low concentration, short time exposure ("low dose"), we aim to look at initial events in this process and particularly those involving the mitochondria.

Human cancer cell lines including A549 (lung adenocarcinoma), PC3 (prostate cancer), and HepG2 (hepatocellular carcinoma), all known to have different mitochondrial activity and metabolism (12, 13), were used in this study. Mitochondrial DNA-depleted derivatives of A549 cells (A549-ρ^0) were also used as a reference because they do not have functioning mitochondrial electron transport chains and hence are incapable of normal oxidative phosphorylation (OXPHOS) (14). In addition to these cell lines derived from cancers, we used BEAS-2B, a noncancer cell line derived from normal bronchial epithelium.

Once the cells were treated with Taxol, we looked at mitochondrial function through optical monitoring of changes in mitochondrial reactive oxygen species (ROS), ATP production, and mitochondrial membrane potential as well as the consequent impact of these changes on ROS-linked protein carbonyl formation, cell cycle, and the release of LDH and cytochrome *c*. Changes in internal mitochondrial oxygen partial pressure (pO_2) and metabolism as well as mitochondrial morphology and transport dynamics (directed flow and random motion) were concomitantly investigated. Mitochondrial pO_2 level *in situ* was measured using fluorescence lifetime imaging (FLIM) of our novel oxygen (O_2) probe, mtMyoglobin-mCherry (15, 16). Changes in metabolic state and redox ratio were also monitored by lifetime imaging of the metabolic cofactors, nicotinamide adenine dinucleotide (phosphate) [H] (NAD(P)H), and flavin adenine dinucleotide (FAD^+). The changes in mitochondrial morphology due to Taxol treatment were studied using the mitochondrial network analysis (MiNA) toolset and the calculation of mitochondrial form factor in ImageJ (17, 18). Mitochondrial directed (flow) and random motions were investigated with temporal and spatiotemporal image correlation spectroscopy (TICS and STICS) (19, 20).

Our results show that Taxol treatment was associated with a multitude of changes in mitochondrial ROS production, membrane potential, morphology, and dynamics. Moreover, we found that Taxol reduced OXPHOS, as seen by a decrease in ATP level, mitochondrial O_2 consumption, and optical redox ratios FLIRR (fluorescence lifetime-based) and ORR (fluorescence intensity-based).

Results

A main result of our work is to bolster the view that Taxol's effects on cell well-being are not limited to a single mechanism linked to microtubule function in mitosis. Rather, since microtubules (or tubulin itself) connect and influence many aspects of cell metabolism, disruption of microtubule dynamics can be expected to have multiple effects. Mitochondria were suggested as potential foci of damage in microtubule disruptions and we pursue that in this paper.

Effects of Taxol on mitochondrial ATP and ROS levels, formation of carbonyl groups, mitochondrial membrane potential, release of cytochrome c and LDH, alteration of cell cycle, and acetylation of tubulin

Mitochondrial density within cells is modulated by factors such as metabolic needs, oxidative stress, and ATP hydrolysis, as well as cell type. As shown in Figure 1*A*, A549 and PC3 cells have higher intracellular MitoTracker intensity when compared to HepG2 cells. Mitochondria have different density, with more crista-membrane surface in those required to produce more energy (21), so finding a smaller contingent of mitochondria in the more glycolytic HepG2 cells is understandable.

Mitochondrial ATP production is the main energy source for intracellular metabolic pathways (22). The human mitochondrial ATP synthase (or OXPHOS complex V) synthesizes ATP from ADP in the mitochondrial matrix using the energy provided by the proton electrochemical gradient. Therefore, measurement of ATP production is a powerful tool to assess mitochondrial function and to detect deficiencies of complex V and other OXPHOS components. We used a luminescent ATP assay kit to detect the changes of mitochondrial ATP production upon Taxol treatment, and we calculated the intracellular ATP level based on the total cell volume and the amount of DNA (stained with Hoechst). As shown in Figure 1*B*, low dose Taxol treatment led to a decrease of intracellular ATP level that was statistically significant in all cell types (p-values ≤ 0.003).

While mitochondria create some ROS as part of their metabolic process for signaling the proper regulation of many essential cellular processes, mutations of complex V can increase ROS production (22). Uncontrolled ROS production

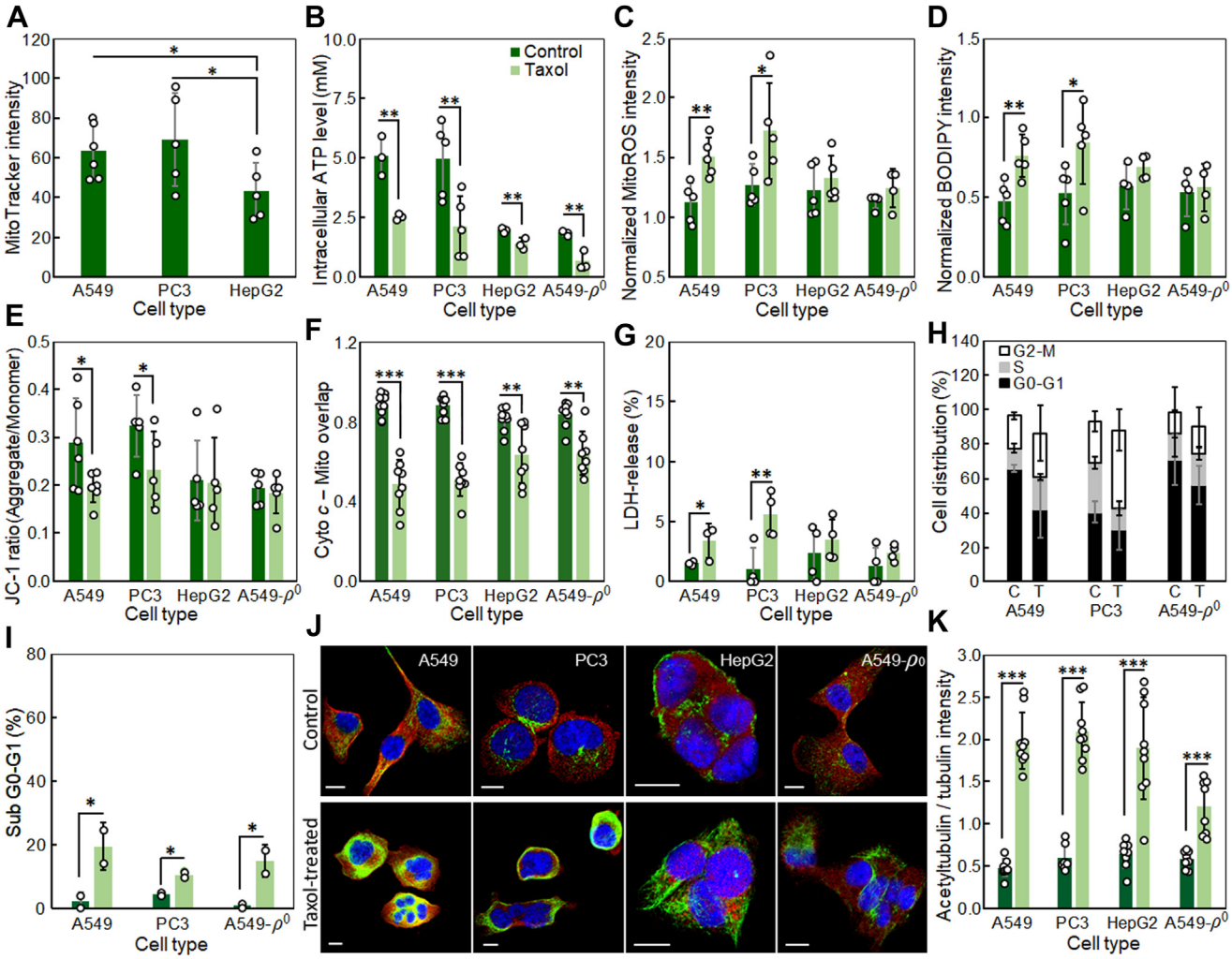

Figure 1. Mitochondrial and cellular effects of Taxol. *A*, intracellular MitoTracker intensity, *B*, mitochondrial ATP, *C*, mitochondrial reactive oxygen species (ROS), *D*, formation of carbonyl groups, *E*, mitochondrial membrane potential, *F*, cytochrome *c* (Cyto *c*)-mitochondria (Mito) overlap coefficient, *G*, cellular LDH release, *H*, cell cycle, *I*, sub G0-G1 distribution, *J*, fluorescence microscopy of acetylation of tubules (nucleus in *blue*, tubulin in *red*, and acetyl tubulin in *green*), *K*, the ratio of acetyl tubulin/tubulin intensity in control and Taxol-treated cells; control refers to cells with no Taxol treatment. Error bars are the SD and individual data points are technical/biological replicates. One-tailed *t* test was used for the statistical analyses. Scale bars in (*J*) are 10 μm. The statistical significance was defined at $p < 0.05$ (95% confidence level); *** for *p*-value <0.001, ** for *p*-value <0.01, and * for *p*-value <0.05.

can lead to changes in the mitochondrial membrane potential and modification or degradation of cellular components such as DNA, proteins, lipids, and carbohydrates. Cumulative effects of this degradation can result in the loss of cell function and/or cell death. Therefore, the detection of changes in mitochondrial ROS is of great importance. We employed the indicator MitoROS to detect the changes of mitochondrial ROS generation due to Taxol treatment; the fluorescence intensity was normalized to the amount of DNA. As shown in Figure 1*C*, Taxol treatment increased MitoROS intensity by ∼34 to 35% in A549 and PC3 cells and ∼8 to 10% in HepG2 and A549-ρ^0 cells. However, these changes were only statistically significant in A549 and PC3 cells (*p*-values ≤ 0.03).

We showed that Taxol increased mitochondrial ROS, and we know from previous studies that Taxol increases superoxide, hydrogen peroxide, and nitric oxide (23, 24). If ROS and other radicals are present, they are expected over time to react with proteins (and certain lipids) to form carbonyl groups (25). To detect the accumulation of carbonyl groups, cells in multiple wells were stained with BODIPY FL hydrazide, which exhibits bright green fluorescence upon reaction with protein or lipid carbonyls; the BODIPY intensity was normalized to the amount of DNA. As shown in Figure 1*D*, treatment with Taxol increased BODIPY intensity by ∼60% in A549 and PC3 cells and ∼6 to 22% in HepG2 and A549-ρ^0 cells (reflecting an increase in the formation of carbonyl groups). Again, however, the increases were only statistically significant in A549 and PC3 cells (*p*-values ≤ 0.03). This measurement integrates nitric oxide and superoxide production over all prior time (26).

Normal mitochondrial membrane potential is necessary for OXPHOS and its ATP production; it is thus essential for maintaining normal mitochondrial function (27). In damaged mitochondria, both OXPHOS activity and mitochondrial membrane potential decrease. We qualitatively measured the effect of Taxol on mitochondrial membrane potential using JC-1, which fluoresces green at low mitochondrial membrane potential (monomer conditions) and orange with high mitochondrial membrane potential (aggregate conditions). Based

on our results shown in Figure 1*E*, Taxol treatment reduced the indicator orange/green intensity ratio by approximately 28 to 32% in A549 and PC3 cells and 2 to 6% in HepG2 and A549-ρ^0 cells; the decreases were only statistically significant for A549 and PC3 cells (p-values < 0.05). The changes in the mitochondrial membrane potential between Taxol-treated and control cells show a general trend of less energized mitochondria in treated cells. This implies an increased proportion of depolarized mitochondria in Taxol-treated cells. In agreement with a previous study (28), JC-1 showed a significantly lower mitochondrial membrane potential for A549-ρ^0 cells (with or without Taxol treatment) when compared to A549 cells (p-values = 0.034).

Mitochondrial membrane permeabilization and the consequent release of cytochrome *c* is an excellent indicator of apoptotic cell death in cancer cells. The mitochondrial localization and release of cytochrome *c* in Taxol-treated cells *versus* nontreated control cells was investigated by immunocytochemistry, fluorescence microscopy, and calculation of the mitochondria-cytochrome *c* Mander's overlap coefficients; an overlap coefficient close to 1 indicates no/less release of cytochrome *c*. A large overlap coefficient calculated for cytochrome *c* and mitochondria shown in Figure 1*F* indicates that cytochrome *c* remained localized within mitochondria of control cells. In contrast, Taxol-treated cells exhibited a more diffuse cytoplasmic staining pattern with cytochrome *c* and lower overlap coefficient between cytochrome *c* and mitochondria (microscopy images in Fig. S2*A* in the Supporting Information). Results show ∼35 to 38% decrease in overlap in A549 and PC3, ∼24% decrease in HepG2, and ∼19% in A549-ρ^0 cells. Significantly, when loss of cytochrome *c* was plotted against DNA content (Hoechst intensity) cell-by-cell, it was found that the effects of Taxol were targeted to cells with G2 level of DNA, that is, cells that have completed DNA replication (Fig. S2*B* in Supporting Information). HepG2 cells appear to be an exception to this, in which cytochrome *c* loss appears to happen in cells at any point in the cell cycle, that is, not correlated with DNA content.

To further study cell damage and cytotoxicity due to Taxol treatment, the release of LDH into the cell culture media was also investigated using an LDH-cytotoxicity assay kit. As shown in Figure 1*G*, Taxol-treated A549 and PC3 cells exhibit a significantly greater number of cells with damaged plasma membranes (3–6%) *versus* their untreated counterparts (p-values < 0.05); Taxol did not cause any significant LDH release in HepG2 and A549-ρ^0 cells. Nonetheless, the release of LDH was found in a small fraction of cells, whether treated with Taxol or not.

We showed that 18 h incubation of the cells with 10 nM Taxol increased cytochrome *c* and LDH release in A549 and PC3 cells. Fluorescence-activated cell sorting (FACS) analysis of the cell cycle and imaging of acetyl tubulin were done to further investigate the mechanism of low-dose Taxol treatment. As shown in Figure 1, *H* and *I*, FACS revealed that the mechanism involves inhibition of mitosis (increased G2/M) and an increase of sub G0/G1 (see Fig. S3 and Table S1 in the Supporting Information for the cell cycle map and mitotic arrest). Based on the fluorescence imaging of acetyl tubulin (green fluorescence) and tubulin (red fluorescence) shown in Figure 1*J* and the intensity ratio of acetyl tubulin/tubulin in Figure 1*K*, Taxol increased microtubule acetylation and stabilized microtubules in all cell types.

Limited studies were also done with an immortalized and noncancer human bronchial epithelial cell line (BEAS-2B) to determine if low-dose Taxol (10 nM, 18 h) has lower activity on the mitochondria of these noncancer cells. Based on our results, the production of mitochondrial ROS and the formation of carbonyl groups in the Taxol-treated BEAS-2B cells were slightly higher than control cells (see Fig. S4, *A–B*). However, only the increase of mitochondrial ROS was statistically significant. A slight (but again, not statistically significant) decrease of mitochondrial membrane potential was measured for Taxol-treated BEAS-2B cells (see Fig. S4*C*). Cytochrome *c*-mitochondria overlap decreased by ∼19% (lower than even A549-ρ^0) and LDH release increased by ∼3% in the Taxol-treated cells (see Fig. S4, *D–E*). Cell cycle was slightly altered (see Fig. S4*F*) by mitotic arrest (Table S1 in Supporting Information) and acetyl tubulin fluorescence increased in the Taxol-treated cells (see Fig. S4*G*).

Changes of mitochondrial pO_2 levels in response to Taxol

The reported reduction of O_2 consumption and the increase in anaerobic glycolytic flux suggests that Taxol, or some downstream effect of Taxol on targets, may act at the mitochondrial level (29, 30), possibly at the level of mitochondrial proteins/protein complexes, including complex V, prohibitins, and voltage-dependent anion channels (31). To investigate this possibility, the effects of Taxol on intramitochondrial pO_2 levels were monitored in A549, A549-ρ^0, PC3, and HepG2 cells at different media-imposed O_2% (from 18.6 to 0.5%) by using lifetime imaging of mtMyoglobin-mCherry, which partitions into mitochondria and reports O_2 levels there (see Fig. 2); all cell types were plated at the same density. This O_2 sensor has a fluorescence lifetime that is based on the oxygenation of myoglobin. When the probe is deoxygenated, its emission intensity and (correspondingly) its lifetime will decrease compared to its oxygenated form (12, 15). The calibration of this O_2 sensor *in situ* was performed by turning off all mitochondrial O_2 consumption by using rotenone/antimycin A inhibitors or A549-ρ^0 cells to nullify OXPHOS (see Fig. S5, *A–D* in the Supporting Information); nonmitochondrial O_2 consumption was then assumed to be negligible due to its small contribution (32). A549-ρ^0 counterparts are auxotrophic for pyruvate and uridine and are also incapable of aerobic respiration due to the lack of key respiratory chain components. Similar to A549-ρ^0 cells, incubating cells with a mixture of inhibitors rotenone/antimycin A or uncoupler 2,4-dinitrophenol resulted in a decline in mitochondrial membrane potential (Fig. S5*A* in the Supporting Information). There also is no statistically significant difference between the lifetime values (apparent O_2) of mtMyoglobin-mCherry in the rotenone/antimycin A–treated cells and A549-ρ^0 cells (Fig. S5*B* in the Supporting Information).

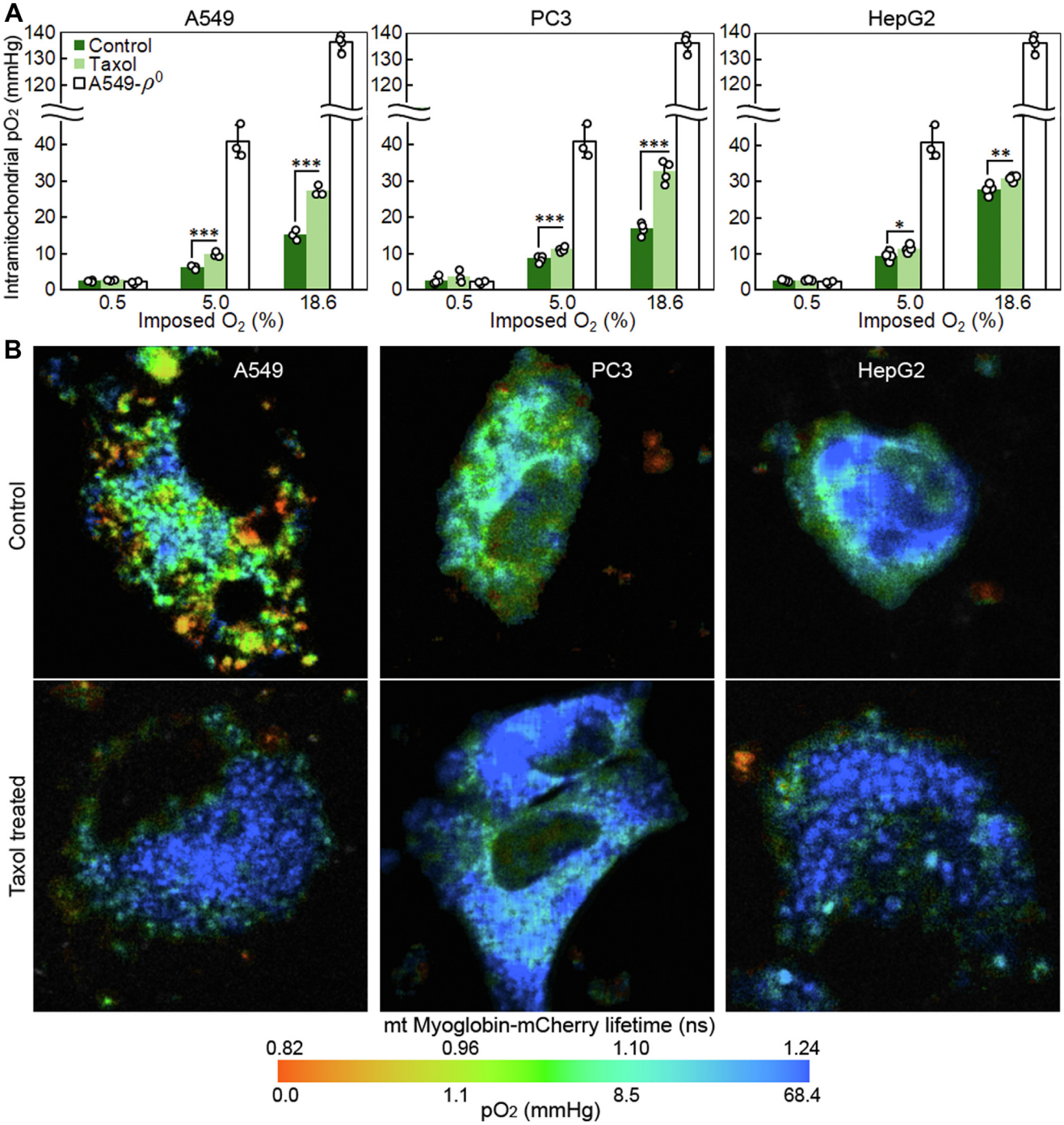

Figure 2. The effects of Taxol on intramitochondrial pO_2 level. *A*, changes in the intramitochondrial pO_2 level of A549, PC3, and HepG2 cells at imposed O_2 of 18.6, 5.0, and 0.5%; data for A549-ρ^0 are included in each panel for comparison. Error bars are the SD and individual data points are technical/biological replicates. *B*, pseudocolor mapping of mtMyoglobin-mCherry lifetime (or pO_2) in the intramitochondrial environment at imposed O_2 of 18.6%. In the color, *red* indicates lower lifetime (or pO_2), whereas *blue* indicates higher values. One-paired *t* test was used to determine if there is a significant difference between the control and Taxol-treated groups. The statistical significance was defined at $p < 0.05$ (95% confidence level); this is represented by *** for *p*-value <0.001, ** for *p*-value <0.01, and * for *p*-value <0.05.

Low O_2 consuming cells, lacking local sinks, are likely to experience greater intracellular pO_2 than those more rapidly consuming O_2 when placed in the same crowded intercellular environment (33). As shown in Figure 2*A*, HepG2 cells yielded higher intramitochondrial pO_2 levels at imposed O_2 of 18.6 and 5% *versus* the other cell types. This is in agreement with previous studies that show HepG2 cells are highly glycolytic (13, 34). Except at hypoxia, where there is no O_2 source for the varying sinks, treatment of the cells with Taxol inhibited mitochondrial metabolic activity in A549, PC3, and HepG2 cells, which was reflected in an increase of the intramitochondrial pO_2 level when compared to untreated cells at the same imposed O_2% (*p*-values ≤ 0.001 for A549 and PC3 cells and *p*-values ≤ 0.02 for HepG2 cells). For cells at

atmospheric (18.6%) imposed O_2, the maximum intramitochondrial pO_2 increased from 15.2 ± 1.4 to 27.4 ± 1.5 mmHg for A549 cells and from 17.1 ± 1.7 to 32.7 ± 3.0 mmHg for PC3 cells. Taxol had a smaller impact on the intramitochondrial pO_2 level of HepG2 cells; the pO_2 increase was from 27.8 ± 1.5 to 30.9 ± 0.8 mmHg at imposed O_2 of 18.6%. The pseudocolor mapping of mtMyoglobin-mCherry lifetime of pO_2 in the intramitochondrial environment of a typical untreated (control) and a Taxol-treated A549, PC3, and HepG2 cell at 18.6% imposed O_2 condition is shown in Figure 2*B* in the color bar, red indicates lower lifetime (or pO_2), whereas blue indicates higher values.

Metabolic redox ratio in response to Taxol

When mitochondrial O_2 consumption decreases, OXPHOS capacity is reduced and glycolysis is enhanced in various cancer cells (35). Changes in metabolism result in changes in NAD^+/NAD(P)H ratios which can be related to the ratio of free to protein-bound NAD(P)H (36). A shift towards the higher free NAD(P)H, and hence a lower NAD^+/NAD(P)H ratio, is indicative of a "more glycolytic" metabolism and a reverse shift is indicative of more OXPHOS. These changes are important for cancer cells, where normal metabolism can be modified by the Warburg effect (36).

With lifetime-based pO_2 measurements, we found that Taxol induced a higher intramitochondrial pO_2 (signaling less consumption) in cultured A549, PC3, and HepG2 cells. This observation prompted us to examine the effects of Taxol on cellular metabolism using optical redox ratios (ORR and FLIRR) obtained by the lifetime imaging of NAD(P)H and FAD^+ (as a proxy of NAD^+) autofluorescence at different imposed O_2% (from 18.6 to 0.5). As A549-ρ^0 mitochondria cannot support normal OXPHOS (14), the NAD(P)H and redox ratios in A549-ρ^0 cells were used for comparison.

We used the pseudocolor mapping of the ratio of free/bound NAD(P)H (shown in Figure 3*A*) and the changes of the ratio at different imposed O_2 conditions (shown in Fig. 3*B*) to noninvasively determine the changes in cellular metabolism due to Taxol treatment. A lower free/bound NAD(P)H ratio for A549 cells led us to characterize A549 cells as having lower glycolysis and more active mitochondria capable of higher O_2 consumption when compared to the other cell types. Among the cells with respiring mitochondria, HepG2 cells exhibited higher free/bound NAD(P)H ratios implying glycolytic activity and lower O_2 consumption. The ratio of the free/bound NAD(P)H was generally higher in Taxol treated cells than untreated control cells, except at hypoxia, where the ratio is, by necessity, quite similar between treated and untreated cells. A higher free/bound NAD(P)H ratio under Taxol treated conditions was accompanied by less OXPHOS in all cell types. However, in agreement with a previous study (37), our measurements showed a decrease of the total NAD(P)H

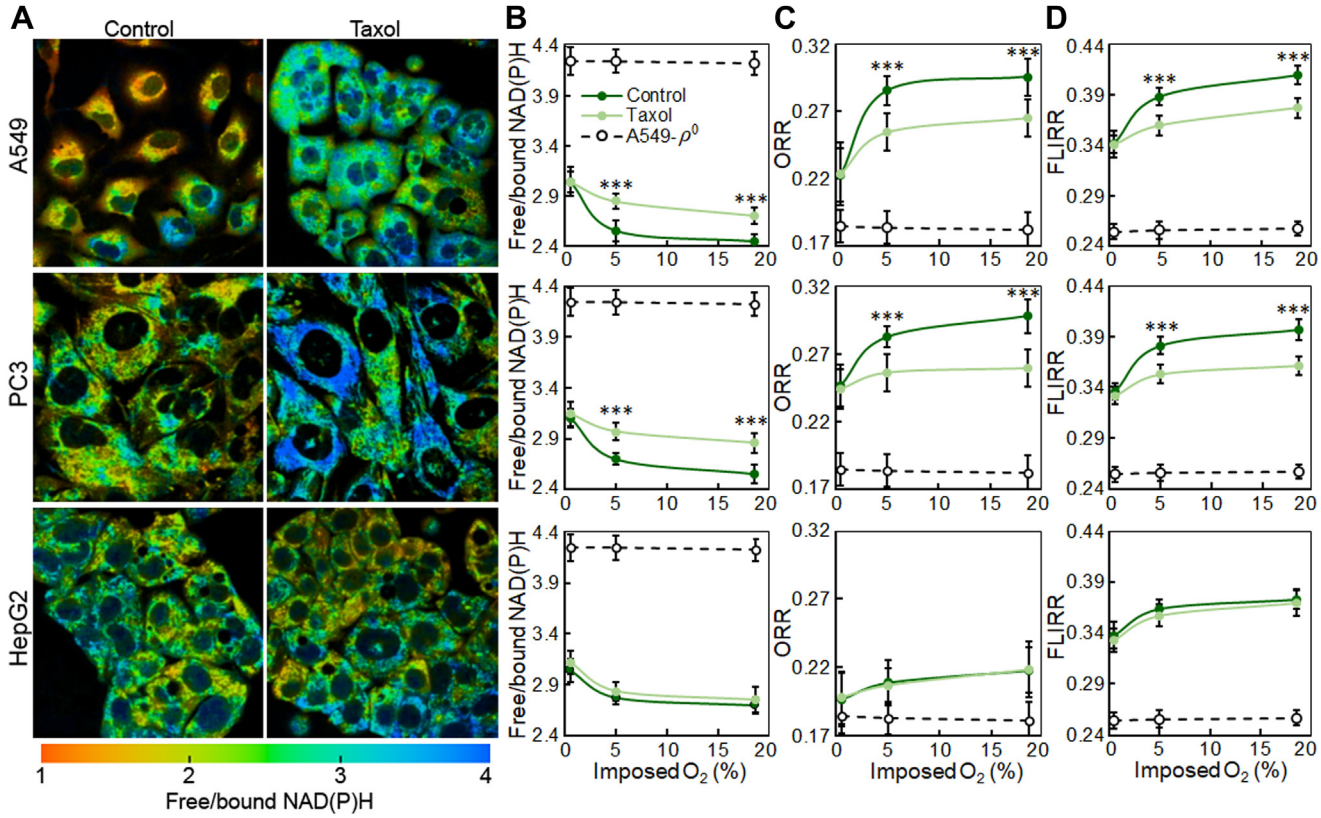

Figure 3. The effects of Taxol on cell metabolism. *A*, pseudocolor mapping of free/bound NAD(P)H in the intracellular environment of untreated (control) and Taxol-treated A549, PC3, and HepG2 cells at atmospheric O_2. The effects of Taxol on the intracellular levels of *B*, free/bound NAD(P)H, *C*, optical redox ratio (ORR), and *D*, fluorescence lifetime-based redox ratio (FLIRR) in A549, PC3, and HepG2 cells at imposed O_2 of 18.6, 5.0, and 0.5%; data for A549-ρ^0 are included (*dashed* lines) in each panel for comparison. Error bars are the SD. Mann-Whitney U test was used to determine if there is a significant difference between the control and Taxol-treated groups. The statistical significance was defined at $p < 0.05$ (95% confidence level); this is represented by *** for *p*-value <0.001.

concentration (maximum 10% in hypoxia) in the Taxol-treated cells (Fig. S6*A* in Supporting Information). The maximum increase of the free/bound NAD(P)H due to the Taxol treatment (∼10–11% at the imposed O_2 of 18.6%) was measured for A549 and PC3 cells. The differences between the free/bound NAD(P)H in the Taxol treated and untreated A549 and PC3 cells were statistically significant (p-values ≤ 0.002) except at hypoxia. The differences between Taxol-treated and control HepG2 cells, presumably due to their already glycolytic character, were not statistically significant at any level of imposed O_2%. As expected, the ratio of free/bound NAD(P)H in A549-ρ^0 cells (dashed lines) was at its maximum and Taxol treatment did not change the ratio (Fig. S6*B* in Supporting Information).

Changes in the redox ratio can be attributed to a change in the free/bound NAD(P)H ratio but is also evinced by a change in the relative amount of NAD(P)H/NAD^+ or FAD^+/(FAD^+ + NAD(P)H) *via* intensity ratio (38). To investigate the effects of Taxol on the redox ratio, ORR was calculated from the FAD^+ and NAD(P)H fluorescence intensity ratio; the intensity was normalized to account for photomultiplier tube gain and the laser power. The results shown in Figure 3*C* show a consistent lower ORR at both 5% and 18.6% imposed O_2 for Taxol-treated A549, PC3, and HepG2 cells compared to their respective controls. The measured ORR for the treated and control HepG2 cells was not statistically different at any of the imposed O_2%. A reduced ORR reflects dominance of glycolysis in Taxol-treated cells at 5% and 18.6% imposed O_2. ORR at hypoxia (0.5% O_2) is about the same for Taxol-treated and untreated cells of the same type. As expected, ORR in A549-ρ^0 cells (dashed lines) was at its minimum and it did not change after the Taxol treatment (Fig. S6*C* in Supporting Information).

ORR requires careful correction for factors that alter intensity at differing wavelengths of excitation and emission; fortunately, intensity independence is true over large ranges for lifetime. As shown in Figure 3*D*, "FLIRR" was also calculated from the ratio of fractional amplitudes of the bound decay components of NAD(P)H and FAD^+ (39). Lifetimes and the lifetime ratio are not concentration dependent and are thus considered a more robust indicator of the metabolic state. FLIRR is also independent of the laser power, focus, and many other instrument parameters. Based on the results shown in Figure 3*D*, at biologically relevant (5%) and atmospheric (18.6%) imposed O_2, the control cells show higher FLIRR than Taxol-treated cells for A549 and PC3 cells, indicating an increase in glycolysis in Taxol-treated cells. HepG2 cells show no difference in metabolism between treated and control cells. A similar trend is depicted in the FLIRR data as ORR with hypoxic conditions showing no significant change in Taxol-treated and untreated cells across all three cell types. The ORR and FLIRR differences between the Taxol-treated and untreated A549 and PC3 cells were statistically significant (p-values ≤ 0.008) except at hypoxia. The measured redox ratios for the treated and control HepG2 cells were not statistically different at any of the imposed O_2%. As expected, the highest anaerobic glycolysis was accompanied by the lowest FLIRR in A549-ρ^0 cells. The treatment with Taxol did not have any significant impact on FLIRR in A549-ρ^0 cells; a comparison of FLIRR in Taxol-treated and untreated A549-ρ^0 cells is shown in Figure S6*D* in Supporting Information.

In our limited studies with the noncancer BEAS-2B cells, a lower free/bound NAD(P)H ratio (2.30–2.39 in BEAS-2B, 2.44–2.55 in A549, and 2.56–2.70 in PC3) and a higher FLIRR (0.41–0.42 in BEAS, 0.38–0.41 in A549 and PC3) at imposed O_2 of 18.6 and 5% led us to characterize BEAS-2B cells as having more active mitochondria capable of higher O_2 consumption and more OXPHOS when compared to the cancer cells. Unlike with cancer cells, however, Taxol treatment did not provide any significant changes in the free/bound NAD(P)H ratio, metabolic redox ratios (ORR or FLIRR), or NAD(P)H concentration at an imposed O_2 of 0.5, 5, and 18.6% (see Fig. S4, *H*–*K*).

Changes of mitochondrial morphology, flow, and random motions in response to Taxol

Mitochondria use microtubule-based mechanisms to migrate throughout the cell *via* both directed transport (flow) and random motion; they also fuse, divide, and undergo regulated turnover, influencing many cellular functions (40, 41). A mitochondrion can either move continually over a long distance at a relatively constant speed or in can pause sporadically and start again with a different speed or direction. These dynamic processes regulate mitochondrial function by enabling mitochondrial recruitment to critical subcellular compartments, content exchange between mitochondria, mitochondrial shape control, and communication with the cytosol as well as mitochondrial quality control. As a result, mitochondria can readily adapt to changes in cellular requirements, whether due to physiological or environmental imperatives (29). Here we discuss the effects of Taxol on mitochondrial morphology, mitochondria associations with microtubules, and mitochondrial dynamics (random walk and flow).

Several time-series images of the mitochondria (labeled with MitoTracker Green) were recorded for the Taxol-treated and control cells. The MiNA toolset identified and characterized morphological changes of mitochondrial networks resulting from the Taxol treatment. As shown in Figure 4*A*, MiNA revealed that the footprint of the mitochondrial network was significantly enlarged in A549, PC3, and HepG2 cells treated with Taxol (p-value ≤ 0.04); mitochondrial footprint is the area of the image consumed by mitochondrial signal. MiNA also showed that mitochondria formed less branched networks in the Taxol-treated cells (Fig. 4*B*), but the changes between the treated and untreated cells were only statistically significant in A549 and PC3 cells (p-value ≤ 0.04). Using a method described previously (18), form factor (inverse of circularity) was also calculated to study the possible mitochondrial fragmentation due to Taxol treatment; form factor describes a particle's shape complexity, with a minimum value of 1 indicating a perfect circle. As shown in Figure 4*C*, form factor decreased significantly in Taxol-treated A549 and PC3 cells reflecting some

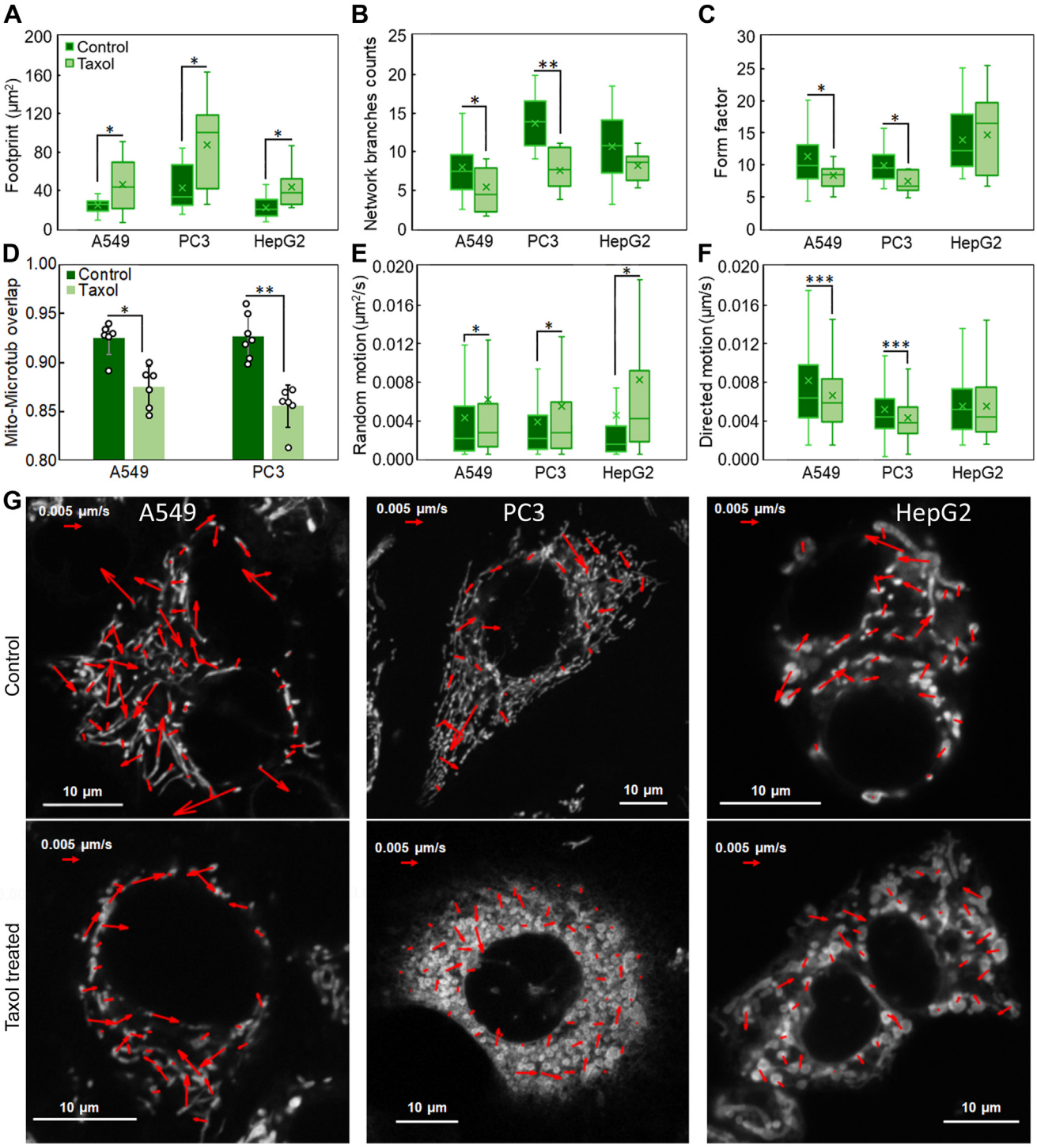

Figure 4. The effects of Taxol on mitochondrial morphology and dynamics. Changes in the mitochondrial *A*, footprint, *B*, number of branch networks, and *C*, form factor. *D*, the alterations of mitochondria (Mito)-microtubules (Microtub) associations in Taxol-treated A549 and PC3 cells. Mitochondrial *E*, random motion and *F*, directed motion (flow) in A549, PC3, and HepG2 cells treated with Taxol. Error bars are the SD and individual data points on bar graphs are biological replicates. Mann-Whitney U test was used to determine if there is a significant difference between the control and Taxol-treated groups. *G*, representative images with flow mapping resulting from STICS analysis of the mitochondria in the intracellular environment of control and Taxol-treated cells. The velocity scale arrows are 0.005 μm/s, and the scale bars are 10 μm. The statistical significance was defined at $p < 0.05$ (95% confidence level); this is represented by *** for *p*-value <0.001, ** for *p*-value <0.01, and * for *p*-value <0.05.

sort of mitochondrial fragmentation. This was not observed in HepG2 cells (Fig. 4*C*), A549-ρ^0 cells (Fig. S7*A*), or in the noncancer BEAS-2B cells (Fig. S4*L*).

Several superresolution z-stack images of the microtubules (labeled with ViaFluor 488) and mitochondria (labeled with MitoTracker Red) in Taxol-treated and control cells were recorded to investigate the possible dissociation of microtubule/mitochondria attachment due to Taxol treatment. While interphase mitochondria associate with microtubules, mitotic mitochondria dissociate from spindle microtubules and

localize in the cell periphery (42). Therefore, we avoided imaging of mitotic cells in both Taxol-treated and control cells. As shown in Figure 4*D*, a smaller 3D Mander's overlap coefficient for the Taxol-treated A549 and PC3 cells indicates an alteration of mitochondria-microtubule association. Taxol did not cause any significant dissociation of microtubule/mitochondria attachment in A549-ρ^0 cells (Fig. S7*B*) or in the noncancer BEAS-2B cells (Fig. S4*M*). Microscopy images of mitochondria-microtubule association is shown in Figure S7*C* in the Supporting Information.

Note that overlap coefficients may be difficult to predict in a heavily crowded scene; while we exploited high 3D resolution to reduce the incidence of accidental overlap, the Mander's overlap changes we report are only meant to be qualitative. Developing methods to better quantify contact frequency are beyond the scope of this study.

The quantification of changes in mitochondrial directed versus random motion between treated and untreated cancer cell-lines was done using STICS and TICS. STICS and TICS are both fluorescence-based microscopy techniques that are appropriate for the study of biomolecular interactions and the measurement of molecular diffusion and flow on time scales ranging from microseconds to milliseconds (19, 20). The correlation analysis of the fluorescence fluctuations in time recorded in the pixels of each image time series (using TICS) allowed us to determine the mitochondrial random motion throughout the cell. A comparison of the box plots of the distribution of the mitochondrial diffusion in the Taxol-treated and control cells shown in Figure 4*E* indicates that mitochondrial random motion increases significantly in response to Taxol (p-value ≤ 0.03).

STICS correlates fluorescence fluctuations in space and time and it depends on both random motion and flow directions of fluorescently tagged mitochondria, enabling us to map the flow velocity vectors (19). A comparison of the box plots of the mitochondrial flow distribution in Figure 4*F* indicates that mitochondria have an average flow at a lower velocity in response to Taxol treatment. However, this change of the mitochondrial velocity was only statistically significant in A549 and PC3 cells (p-value ≤ 0.0006). A velocity mapping example of the mitochondria flowing in the intracellular environment of the control and Taxol-treated A549, PC3, and HepG2 cells is shown in Figure 4*G*.

Measurements of mitochondrial dynamics in the noncancer BEAS-2B cells showed no changes in their random motion in response to Taxol treatment (see Fig. S4*N*). However, a significant decrease of mitochondrial directed motion was detected in the Taxol-treated cells (see Fig. S4*O*).

Discussion

Summary and comparison of data

In order to facilitate comparison of the data, we combined data from the previous sections into a table based on the changes observed in each parameter by incubation with Taxol (see Figure 5). This "heat map" facilitates comparisons that show several things. The top section, effects targeting microtubules, shows that Taxol enters all of the cell types and produces the expected results on the microtubule network: stabilizing individual microtubules (acetylation of tubulin) and accumulating cells in mitosis (mitosis numbers are from the FACS studies shown in Fig. S3 or a microscope replication). The mitochondria section shows that Taxol effects on mitochondrial properties are not uniform like microtubule effects but rather are significantly altered in oxidative cancer cells, but not so much in glycolytic cancer cells. Oxidative noncancer cells behave like glycolytic cancer cells, showing only modest response to Taxol. The physiology section shows that Taxol effects on whole-cell properties are also more profound in oxidative cancer cells than in glycolytic cancer cells. Again, oxidative noncancer cells show modest response to Taxol, like glycolytic cancer cells.

Effects of Taxol treatment on the mitochondria

Taxol is known to reduce the propagation of cells by targeting microtubule structures and thus altering the formation and function of microtubule arrays. Initially, Taxol was thought to impede cell division only by increasing the mass of microtubules in the cell and decreasing their dynamicity—thus, eliminating the cell's ability to divide and multiply (43). Interestingly, Taxol's effectiveness as a chemotherapy drug does not rely principally on inhibition of mitosis, indicating that other cell functions are targeted by Taxol besides mitosis (44). Microtubules have many functions in the cell beyond cell division. For example, it has been proposed that mitochondria use microtubule networks as railways to translocate within cells (29). Thus, the impact of Taxol interrupting and altering microtubules may have additional deleterious implications on cell health and function. Although Taxol does act as a mitotic inhibitor in rapidly growing cells, at lower concentrations, the drug still effectively targets some cell process(es), possibly through inhibition of some interactions between cytoskeletal components and the mitochondrial network. Treatment with Taxol was shown here to correlate with increased ROS, suppression of ATP production and OXPHOS, and a decrease in mitochondrial health by several indicators, which could result in significantly decreased metabolic capacity. It is possible that the effects of Taxol on mitochondria lead toward cell death by many pathways at once, each a potential secondary mechanism of the drug. This has not been deeply investigated. Taxol may induce the dissipation of mitochondrial membrane potential and open the permeability transition pore (either enzymatically and/or through interaction with cytoskeletal elements) (45). The opening of inner membrane pores causes equilibration of ions within the matrix and the cytosol, decreasing the mitochondrial membrane potential and impairing the respiratory chain, with subsequent disruption of OXPHOS activity and cellular energetics. Any volume dysregulation following this opening of the permeability transition pore results in the swelling of the matrix, potentially leading to outer membrane disruption and the release of cytochrome *c*, cytochrome oxidase–mediated ROS, and other caspase-activating proteins into the cytosol. Because both cytochrome *c* release

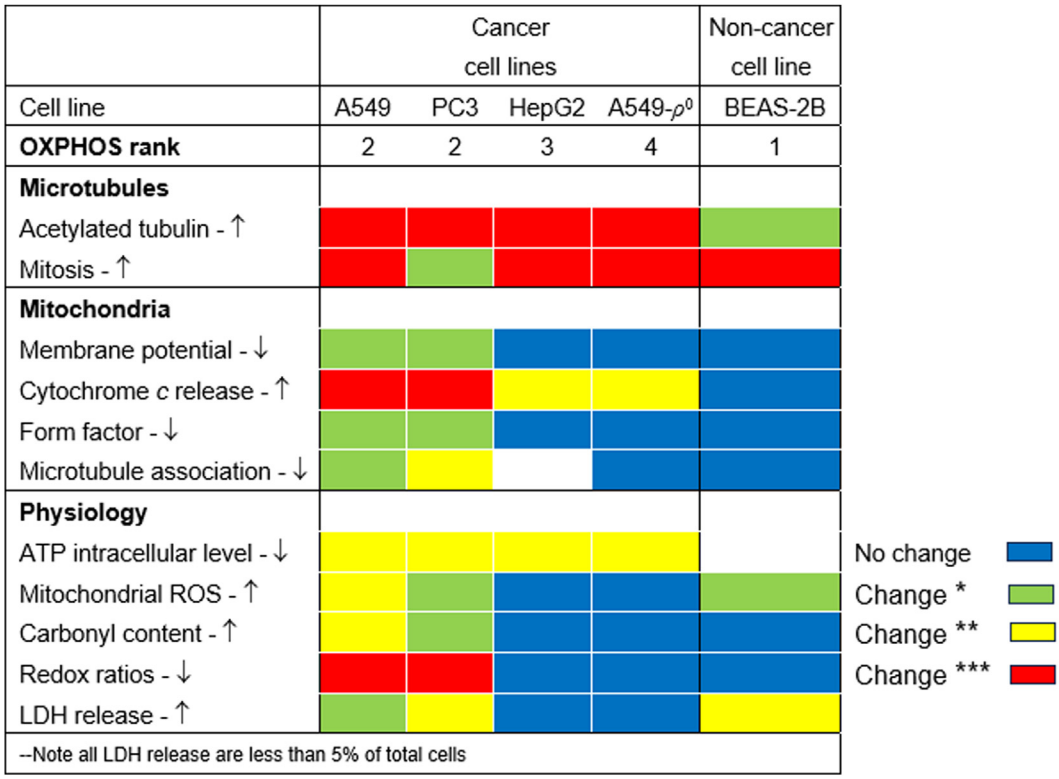

Figure 5. Comparison of effects of Taxol on the parameters measured. Results are presented in a heat map arranged by cell type and by the locus of Taxol effect. Cells are arranged as cancer cells, followed by noncancer cells. Within these blocks, cell lines are arranged by oxidative to glycolytic (L to R), in order given by the "OXPHOS rank." Parameters are arranged vertically based on the target of the effect measured: effects on microtubules, effects on mitochondria, and effects on whole cell physiology. Each cell in this matrix is colored based on statistical significance of the change indicated.

and mitochondrial ROS production can induce suicide pathways, mitochondrial effects of Taxol may contribute to its cytotoxicity and ultimately contribute to cell apoptosis (45, 46). The altered membrane potential of mitochondria due to Taxol treatment may also affect the various proteins regulating mitochondrial motion, fission, and fusion, which are all necessary activities for maintaining the health of the mitochondrial network. Further, a decrease in the mitochondrial membrane potential has been previously shown to correspond with an increased level of mitophagy (47), which further dismantles the mitochondrial network. The balance between fission and fusion within the mitochondria has also been shown to be critical for regulating cell death and an imbalance may lead to apoptosis (48). Irregular fission and fusion have also been connected to decreased mitochondrial motility, which in turn has been related to decreased metabolic capacity (49). Finally, the decreased motility, an increase in random movement and inhibition of the cytoskeleton could indicate a failure of the cell to localize the mitochondria to regions of the cell with high metabolic needs, a behavior which is crucial for preventing cell death (46). Together, these phenomena would indicate that Taxol has a detrimental effect on the health of the mitochondrial network by inhibiting mitochondrial dynamics and interaction with the cytoskeleton. Although impeded mitochondria may not be the primary cause of cell death by Taxol, its efficacy at lower doses through secondary interactions with the mitochondria needs to be fully investigated.

Clinical relevance

Cancer recurrence or resistance to therapy often results from the cooperation of several cellular defense mechanisms, which may be connected to mitochondria. Many clinical trials are underway to assess the effectiveness of inhibiting mitochondrial respiration and/or changes in glycolysis as a potential cancer therapeutic. Currently, increasing evidence suggests that increased aerobic glycolysis is closely associated with chemotherapy (*e.g.* Taxol) resistance, even under O_2-rich conditions (50, 51). Changes in glycolysis particularly increases key enzymes and intermediates of this pathway. This can affect the sensitivity of tumors to chemotherapeutic reagents, resulting in an increase in ATP production, and providing sufficient energy for the biological activity of tumor cells (50).

In this study, we used innovative strategies and techniques based on FLIM and image correlation spectroscopy to study the impact of Taxol on mitochondrial respiration, dynamics, and morphology. As the principal organelles of cellular energy conversion, mitochondria can rapidly alter cellular metabolic processes, thereby fueling malignancies and contributing to treatment resistance. Since glycolysis is the fundamental cellular process that permits cancer cells to convert energy and grow anaerobically, our study emphasizes the significance of mitochondrial dynamics, morphology, and pO_2 level to the treatment response. The fact that Taxol affects these basic metabolic processes of the cell through the mitochondria may suggest that a combination of Taxol with specific

mitochondrial targeting agents may provide synergy in targeting cancer cells or at least ones with functioning mitochondria. However, this sort of inquiry is considerably beyond the scope of the current work.

Note that our study addresses the mechanisms of dysregulation that happen in cultured cells exposed to constant, low doses of Taxol for short periods. Clinical therapy usually utilizes much higher concentrations that vary quite significantly over longer periods of time.

In this study, we showed that HepG2 and A549-ρ^0 cells exhibited less mitochondrial O_2 consumption and higher aerobic glycolysis as compared to epithelial A549 and PC3 cancer cells. Higher glycolysis was associated with increased intramitochondrial pO_2 level, higher free/bound NAD(P)H ratio, and lower metabolic redox ratios. This might explain why low-dose Taxol has the least impact on intramitochondrial oxygenation, optical redox ratio, and proliferation of such glycolytic HepG2 cells. The resistance of the oxidative, noncancer-derived BEAS-2B cells to low dose Taxol effects on many mitochondrial markers demonstrates that a simple oxidative/glycolytic switch is not dispositive for cell sensitivity/resistance.

Conclusions

In this study, we reported on the effects of low-dose Taxol on mitochondrial energetics, oxidative damage, and intracellular migration patterns. We observe (by multiple optical means) suppression of OXPHOS and decrease of ATP production, increase of ROS generation (both immediately and integrated over time), increased mitotic fraction, and release of LDH and cytochrome *c* in Taxol-treated cells. Moreover, we observed more random (less ordered) motion of the mitochondria as well as altered mitochondrial morphology and lessened association with microtubules.

The cell lines used were found to vary from oxidative to glycolytic according to BEAS-2B > A549 = PC3 > HepG2 > A549-ρ^0. Taxol effects also varied in the same order, with the notable exception being noncancer human bronchial epithelial BEAS-2B cells; they had minimal sensitivity to mitochondrial effects of Taxol, similar to the glycolytic cancer cell lines. This is true not only of Taxol effects directly focused on the mitochondria, such as loss of mitochondrial membrane potential, but also for Taxol effects not closely linked to mitochondria, such as loss of cytoplasmic LDH.

Tubulin and microtubules are undeniably the proximal target of Taxol and cognates, and we show that all of the cell lines are similarly sensitive to direct effects on microtubules (stabilization of microtubules and mitotic arrest). We suggest that microtubule dynamics are essential to normal mitochondrial function and that interruption of these dynamics, even with low doses of Taxol, suffice to induce mitochondrial dysfunction. We speculate this may explain why Taxol can still be effective against tumors that contain few mitotic cells, since nondividing cells still require functioning mitochondria. Moreover, our study suggests a need to examine the broader mechanisms of Taxol, especially at low doses, and the techniques used herein are applicable to the further study of mitochondrial dynamics and the wider study of cellular dynamics.

Experimental procedures

Cell culture

A549, PC3, HepG2, and BEAS-2B cells were kept in Dulbecco's Modified Eagle's Medium with 10% fetal bovine serum and 1% penicillin-streptomycin (Mediatech Inc). A549-ρ^0 cells were kept in Dulbecco's modified Eagle's medium supplemented with sodium pyruvate (1 mM) and uridine (50 μg/ml). The cells were plated in μ-Slide 8-well chambers (Ibidi GmbH) or in 96-well microplates (Costar Assay Plate, Clear, Easywash Bottom, Corning) with a density of 1 to 2 × 10^4 cells/cm^2.

A549 and PC3 cells were obtained from NCI Cell Screen, and HepG2 and BEAS-2B cells were obtained from ATCC. A549-ρ^0 was derived from the A549 cells and is confirmed by the continuing absence of mitochondrial DNA and inability to grow in the absence of uridine supplementation. All cells were used within 25 passages from receipt, and absence of *mycoplasma* was confirmed by routine fluorescence microscopy.

Analysis of LDH release

Taxol stock solution (100 μM) was made in dimethyl sulfoxide (DMSO) and diluted with cell culture media to yield final drug concentrations of 10, 20, 30, and 40 nM. After the treatment of cells with different concentrations of Taxol for 18 or 24 h, the cell damage was studied based on the measurements of LDH released from cells. These measurements were done using LDH-cytotoxicity assay kit (abcam) following the manufacturer's instructions. The cells were additionally treated with 10 μM Hoechst (Thermo Fisher Scientific) to quantify cell density, accounting for the simultaneous effects of Taxol on cell proliferation. A FLUOstar Omega multi-mode microplate reader (BMG LABTECH) was used for the measurements of Hoechst fluorescence with absorption/emission filters of 355-20/460 nm and LDH-cytotoxicity assay absorbance at 490 to 500 nm with a reference wavelength > 600 nm (Fig. S1, *A–D* in Supporting Information). Results are presented as % release, where 100% release is taken as the amount released upon exposure of the cells to medium containing 1% Triton X-100. Based on the results, 18 h exposure to 10 nM Taxol was selected for this study to avoid the implications of cell deformation and movement or intense autofluorescence from cell apoptosis, which can lead to a false fluorescence response in FLIM and time-lapse fluorescence microscopy (52).

Diluting Taxol stock solution into cell culture media brought DMSO to 0.01% v/v, which is widely taken to have no cellular effect. Therefore, cells in their culture media with no Taxol or DMSO were used as controls.

Analyses of mitochondrial ATP and ROS production, mitochondrial membrane potential, and carbonyl formation

Cells in 96-well plates were treated with 10 nM Taxol for 18 h. Following this treatment, the cells in multiple wells were incubated with 1 μM MitoROS 580 (Cayman Chemical),

10 μM BODIPY FL Hydrazide (Thermo Fisher Scientific), or 6 μg/ml of JC-1 (tetraethyl benzimidazolyl-carbocyanine iodide, Thermo Fisher Scientific) for 30 min to detect the mitochondrial ROS, formation of the carbonyl groups, and changes of mitochondrial membrane potential, respectively. The changes of mitochondrial ATP level due to the Taxol treatment was also investigated by using Luminescent ATP detection assay kit (abcam) following the manufacturer's instructions. Control cells were carried through the protocol but not treated with Taxol. Both Taxol-treated and control cells were additionally treated with 10 μM Hoechst (Thermo Fisher Scientific) to normalize the intensity profile and ATP level based on the amount of DNA present in each well. The JC-1 assay is a ratio of orange and green fluorescence, so no normalization was used. The signals were detected using a FLUOstar Omega multimode microplate reader (BMG LABTECH) with absorption/emission filters of 355-20/460 nm for Hoechst, 485-12/520 nm for BODIPY, 485-12/590 nm for MitoROS, and luminescence for ATP. Absorption/emission filters of 485-12/520 nm and 485-12/620 nm were used for the detection of JC-1 monomeric form with green fluorescence and J-aggregates with orange fluorescence.

Imaging of cytochrome c release, tubulin acetylation, and mitochondria-microtubule association

The cells were grown on μ-Slide 8-well removable chamber slides (Ibidi) at a density of 1.5×10^4 cell/cm^2. To detect cytochrome *c* release, the cells were exposed to 10 nM Taxol for 18 h. Following a protocol published previously (53), the cells were then fixed with prewarmed 2% p-formaldehyde for 20 min followed by −20 °C methanol and processed for immunofluorescence by labeling with mouse anti-cytochrome *c* (1:100, BD Pharmingen) and with recombinant rabbit anti-TOM20 (1–100, Invitrogen), followed by appropriate fluorescently labeled secondary antibodies. For imaging of tubulin acetylation, both control and Taxol-treated cells were fixed with −20 °C methanol and processed for immunocytochemistry using anti-acetylated tubulin (1–1000, recombinant Mouse monoclonal 6–11-B1, a kind gift from Dr Kristen Verhey, Univ Michigan) and chicken anti-alpha tubulin (1–500, Sigma, US), followed by appropriate fluorescently labeled secondary antibodies. After washing the sample three times with Tris-buffered saline, Hoechst (10 μM) was added to label the nucleus and the sample was sealed and protected from the light. For mitochondria-microtubule association studies, live Taxol-treated and untreated cells were labeled with MitoTracker Red FM (Invitrogen) and ViaFluor 488 microtubule stain (Biotium).

Cytochrome *c* release and tubulin acetylation were detected using a Zeiss 780 confocal laser scanning microscope (Jena) and 3D images of mitochondria-microtubules association were acquired using a Zeiss 980 Confocal laser scanning microscope equipped with Airyscan (both Jena). The beams from multiple lasers emitting at 405, 488, 568, and 594 nm were directed onto the sample using a Plan-Apochromat 63 × /1.4 NA Oil immersion objective. Then, the fluorescence signals collected from the sample were directed toward proprietary Zeiss photomultiplier tubes and were spectrally filtered by selecting a 415 to 481 nm filter for Hoechst, a 490 to 531 nm filter for cytochrome *c*, 380 to 735 nm for ViaFluor 488, and a 600 to 630 nm filter for the imaging of mitochondria. Then, Mander's overlap coefficient for the colocalization between cytochrome *c* and mitochondria or mitochondria and microtubules was calculated using JACoP toolset in ImageJ (54).

FACS for cell cycle studies

Taxol-treated (10 nM, 18 h) and untreated A549, PC3, BEAS-2B, and A549-ρ^0 cells were fixed with cold methanol, rehydrated, and processed for antibody staining with anti-mitotic marker (anti-histone H3 (pS28)–AF647, BD-Pharmingen). Then, they were stained with propidium iodide (0.05 μg/ml final concentration) overnight to achieve equilibrium. Next day, the cell cycle profiles of Taxol-treated and untreated cells were determined by FACS (BD Fortessa) equipped with 532 and 640 nm laser lines. Propidium iodide was excited by 532 nm laser line and peak emission was detected using 610/20 band pass filter at linear scale, and AF647 was excited using 640 nm laser line and peak emission of signal was detected using 660/40 nm bandpass filter. All samples were recorded at ∼200 events/seconds using FACS-Diva Software (BD). Recorded data was further analyzed using FlowJo v10 software (BD) for identification of cell cycle stages.

Cell transfection with mtMyoglobin-mCherry O_2 sensor

The transfection solution was prepared in antibiotic free Opti-MEM (Gibco) medium using a mixture of Lipofectamine 2000 transfection reagent (Invitrogen) and 200 ng plasmid DNA. After a 15-min period, the DNA–lipofectamine transfection complex was added to the cells in μ-Slide 8-well chambers (Ibidi GmbH). After ∼ 32 h of incubation at 37 °C and 5% CO_2, the transfection media was removed, and the cells were washed and treated with 10 nM Taxol for 18 h. To calibrate the mtMyoglobin-mCherry probe, mitochondrial O_2 consumption was shutdown using a mixture of 2 μM rotenone/antimycin A.

FLIM setup for pO_2 and metabolic imaging

Two-photon FLIM was performed using an Olympus IX81/FV1000 confocal laser scanning microscope (Melville) equipped with a tunable Mai Tai BB DeepSee femtosecond laser (Spectra-Physics) operating at 80 MHz with wavelengths set to 860, 780, and 750 nm for the excitation of FAD$^+$, mCherry, and NAD(P)H, respectively. The excitation light was passed through a 690 nm dichroic mirror and directed to an Olympus UPLANSAPO 60 × , 1.2 NA water immersion objective. The emission was routed to the side port of the microscope (non-descanned detection) and passed through a 675 nm short pass filter to eliminate scattered light. The mCherry, FAD$^+$, and NAD(P)H signals were filtered through 647/57 nm, 560/40 nm, and 460/60 nm bandpass filters (Semrock BrightLine), respectively. The fluorescence was focused on a PMC100 air cooled detector (Becker & Hickl GmbH) and the electrical

pulse from the detector was directed into an SPC-150N photon counting card (Becker & Hickl). Synchronization with the pixel, line, and frame clock from the scanning unit of the microscope was used for image construction in time-correlated single photon counting mode. The cells were excited with IR laser power ≤ 14 mW and imaged for 30 – 50 s to accumulate an adequate number of photons per pixel and to avoid photobleaching and photocytotoxicity. Image size was set to 256 × 256 (pixels)^2, and time-correlated single photon counting histograms were collected with 256 channels in a 12.5 ns time window. Note that the Taxol dose (10 nM/18 h) used in our studies allowed cells to survive at a rate that can support FLIM without concerns of cell deformation and movement or intense autofluorescence from cell apoptosis.

During the live cell imaging, a miniature incubator was mounted on the microscope stage and connected to a gas mixing system (O_2 – CO_2–N_2-MI, Bioscience Tools) to keep the temperature at 37 °C, maintain CO_2 at 5%, and set O_2 at different concentrations from 18.6 to 0.5%; 0.5% is the lowest $\%O_2$ reachable by our system. The cell culture (in dishes with a ∼3 mm layer of medium above cells, without lids) reaches a stable $\%O_2$ within 1 h. The media-imposed external pO_2 (in mmHg) at the deposited cell layer was measured by a 250 μm diameter bare-fiber O_2 sensor (NX-BF/O/E) connected to an OxyLite 1 Channel monitor (Optronix Ltd).

Intracellular mapping of pO_2 and calculation of redox ratios

Using the SPCImage software (Becker & Hickl), fluorescence lifetime decay curves at each pixel were fit *via* iterative reconvolution with a default synthetically generated instrument response function. The decay values were obtained by a double-exponential model at optimized goodness of fit (χ_r^2). Binning of adjacent pixels was used to avoid fitting decays with a peak count lower than 1000, thus retaining Gaussian weighting.

For the mitochondrial pO_2 measurements, the average fluorescence lifetime at each set value of pO_2, $\tau(pO_2)$, was calculated for rotenone/antimycin-treated cells by taking the mean lifetime from each single image and averaging this across multiple cells ($n > 20$). As published previously (12), the resulting lifetime values were plotted against the media-imposed external pO_2, and a hyperbolic curve was fit to the data using the Curve Fitting Toolbox in MATLAB R2022b (The MathWorks Inc.):

$$\tau(pO_2) = (\tau_{max} - 0.92)\frac{pO_2}{K + pO_2} + 0.92 \quad (1)$$

where τ_{max} is the longest average lifetime obtained for mtMyoglobin-mCherry at imposed O_2 of 18.6%; 0.92 ns is the shortest lifetime obtained at hypoxia. K is a fitting parameter related to the affinity of myoglobin for O_2, and we found this to be in the range of 8.51–8.95 for the nonrespiring cells.

Since cells treated with rotenone/antimycin are incapable of significant O_2 consumption, intracellular pO_2 is assumed in this case to be equivalent to the media-imposed pO_2. Therefore, the $\tau(pO_2)$ values for the treated cells can be used as a reference for the lifetime of the probe at the environmental level of pO_2 present in solution; the $\tau(pO_2)$ values of rotenone/antimycin-treated cells and a more detailed description of the calibration curve derived from these lifetime values are shown in Figure S4 in Supporting Information. Rearranging Equation 1, it is possible to back calculate the effective pO_2 at each mean lifetime value for the respiring cells, fixing the K and τ_{max} to the values obtained from the nonrespiring data. Finally, the pseudocolor mapping of mean lifetime and the corresponding mitochondrial pO_2 in the intracellular environment were conducted using the SPCImage software (Becker & Hickl).

A full set of parameters including lifetime values (τ_1 and τ_2), percentage of amplitudes (a_1% and a_2%), and normalized amplitudes ($|a_1|$ and $|a_2|$) for NAD(P)H and FAD^+ were generated *via* amplitude weighting for each pixel to calculate optical redox ratio (ORR) and fluorescence lifetime-based redox ratio (FLIRR). ORR was calculated by using the intensity ratio of FAD^+/(NAD(P)H + FAD^+) and FLIRR was calculated from bound NAD(P)H/bound FAD^+ ($a_{2,NAD(P)H}$ %/a_{1,FAD^+} %).

Measurements of the mitochondrial directed and random motions

After 18 h of incubation with Taxol, mitochondria were labeled with 200 nM MitoTracker Green (Molecular Probes, Eugene) for 20 min at 37 °C and 5% CO_2. Then, the cells were washed and incubated in fresh culture medium for the imaging.

The time-series images of the cells were acquired using a commercial Zeiss 780 Confocal laser scanning microscope (Jena) for TICS and STICS analyses. The beam from a multiline argon laser emitting at 488 nm was directed onto the sample using a dual band dichroic mirror, MBS 488/594, and a Plan-Apochromat 63 × /1.4 NA Oil immersion objective. The green fluorescence collected from the sample was directed toward a Zeiss photomultiplier tube and spectrally filtered by selecting a 490 – 562 nm bandpass filter. All images of each series (60 frames) were collected with no added time delays between the sequential frames. The individual frames (512 × 512 pixels) were acquired with a pixel dwell time of 2.55 μs and the images had a pixel size in the range of 0.06 – 0.19 μm.

TICS and STICS analyses were performed using MATLAB R2022b (The MathWorks Inc.) routines adapted from the works of Wiseman Research group, McGill University (19, 20). The STICS spatiotemporal autocorrelation functions were performed for 32 × 32 pixels subregions of the images. The spatiotemporal component of these correlation functions was averaged and fitted by nonlinear least squares. For the same subregions of the images, the TICS temporal autocorrelation functions were calculated to obtain the magnitude of random motion. Each image correlation analysis was performed at least on 10 cells of the same type with at least eight distinct subregions for each cell.

We strive to keep the laser intensity at the lowest feasible power and to keep the pixel dwell time optimized to prevent cell stress from the measurement itself. However, for each individual cell, STICS analysis was also performed on the

entire cell to account for possible stage drift and any cell movement due to the stress from Taxol treatment and/or ROS generation.

Analyses of the mitochondrial morphology

For morphological studies, the fluorescence images of the mitochondria labeled with MitoTracker Green underwent a preprocessing workflow using contrast limited adaptive histogram equalization and then were converted into binary by thresholding in ImageJ software, where a foreground pixel is assigned the maximum value and background pixels are assigned the minimum possible value. Using the ImageJ built-in "Skeletonize" feature, the binary image is then converted to a skeleton that represents the feature in the original image using a wireframe of lines one pixel wide. MiNA recognizes only two distinct object types: individual (no junctions) and networks (structures with at least one junction). Using the MiNA toolset, each pixel of a skeleton was classified and was spatially related and defined to measure the length of each branch and the number of branches in each skeletonized feature. A more detailed description of the MiNA toolset and analyses can be found elsewhere (17).

To determine mitochondrial form factor, skeletonized images were processed with ImageJ's built in analysis tool "Analyze Particles" to resolve perimeters (p) and areas (a) (18). Then, these parameters were used to calculate the form factor defined as $n^{-1}\sum^{n}\frac{p^2}{4\pi a}$.

Statistical analyses

Multiple cells and/or plate wells were measured in each condition over different days in at least three independent experiments. Bar charts (with individual data points) and line graphs were used to present the mean values with SD. Box plots were also created to visually compare the different sets of data and study means and anomalies at $p < 0.05$ (or 95% confidence level) for the mitochondrial morphology as well as their flow and random motions; organizing these data with large SDs in box plots (with the median and the upper and lower quartiles) was the most efficient way of showing the differences. Mann-Whitney U test or one-tailed t test were carried out using SPSS 14.0 software (IBM) to evaluate whether the values in the independent groups are significantly different from each other; the data were tested for normal distribution using Kolmogorov–Smirnov or mean-variance tests. The statistical significance was defined at $p < 0.05$ (95% confidence level) and was shown with stars on each plot; three stars for p-value < 0.001, two stars for p-value < 0.01, and one star for p-value < 0.05.

Data availability

Data available on request.

Supporting information—This article contains supporting information (53, 55–58).

Acknowledgments—We would like to acknowledge the NHLBI Light Microscopy Core (especially Christian Combs) for use of their confocal microscope for TICS and STICS and the NHLBI Flow Cytometry Core for cell cycle and apoptosis analyses. We also thank our collaborator Jay H. Chung for his insightful feedback.

Author contributions—R. P., K. A. L., A. Z., D. L. S., and J. R. K. writing–review and editing; R. P. and K. A. L. writing–original draft; R. P. and K. A. L. methodology; R. P., K. A. L., S. Q., N. M., A. Z., and A. V. investigation; R. P., K. A. L., S. Q., N. M., A. Z., and A. V. formal analysis; S. Q. visualization; N. M. software; D. L. S. and J. R. K. supervision; D. L. S. and J. R. K. resources; D. L. S. and J. R. K. funding acquisition; D. L. S. and J. R. K. conceptualization.

Funding and additional information—This research was funded by the Intramural Research Program of National Heart, Lung, and Blood Institute (NHLBI) and in part by the Intramural Research Program of the *Eunice Kennedy Shriver* National Institute of Child Health and Human Development (NICHD).

Conflicts of interest—The authors declare that they have no conflicts of interest with the contents of this article.

Abbreviations—The abbreviations used are: DMSO, dimethyl sulfoxide; FACS, fluorescence-activated cell sorting; FLIM, fluorescence lifetime imaging; LDH, lactate dehydrogenase; MiNA, mitochondrial network analysis; OXPHOS, oxidative phosphorylation; ROS, reactive oxygen species; STICS, spatiotemporal image correlation spectroscopy; TICS, temporal image correlation spectroscopy.

References

1. Dai, Q., Liu, X., He, T., Yang, C., Jiang, J., Fang, Y., *et al.* (2021) Excipient of paclitaxel induces metabolic dysregulation and unfolded protein response. *iScience* **24**, 103170
2. Kavallaris, M. (2010) Microtubules and resistance to tubulin-binding agents. *Nat. Rev. Cancer.* **10**, 194–204
3. Zasadil, L. M., Andersen, K. A., Yeum, D., Rocque, G. B., Wilke, L. G., Tevaarwerk, A. J., *et al.* (2014) Cytotoxicity of paclitaxel in breast cancer is due to chromosome missegregation on multipolar spindles. *Sci. Transl. Med.* **6**, 229ra243
4. Poruchynsky, M. S., Komlodi-Pasztor, E., Trostel, S., Wilkerson, J., Regairaz, M., Pommier, Y., *et al.* (2015) Microtubule-targeting agents augment the toxicity of DNA-damaging agents by disrupting intracellular trafficking of DNA repair proteins. *Proc. Natl. Acad. Sci. U. S. A.* **112**, 1571–1576
5. Smith, E. R., and Xu, X. X. (2021) Breaking malignant nuclei as a non-mitotic mechanism of taxol/paclitaxel. *J. Cancer Biol.* **2**, 86–93
6. Khing, T. M., Choi, W. S., Kim, D. M., Po, W. W., Thein, W., Shin, C. Y., *et al.* (2021) The effect of paclitaxel on apoptosis, autophagy and mitotic catastrophe in AGS cells. *Sci. Rep.* **11**, 23490
7. Jordan, M. A., Toso, R. J., Thrower, D., and Wilson, L. (1993) Mechanism of mitotic block and inhibition of cell proliferation by taxol at low concentrations. *Proc. Natl. Acad. Sci. U. S. A.* **90**, 9552–9556
8. Yvon, A. M., Wadsworth, P., and Jordan, M. A. (1999) Taxol suppresses dynamics of individual microtubules in living human tumor cells. *Mol. Biol. Cell.* **10**, 947–959
9. Shi, X., Jiang, X., Chen, C., Zhang, Y., and Sun, X. (2022) The interconnections between the microtubules and mitochondrial networks in cardiocerebrovascular diseases: implications for therapy. *Pharmacol. Res.* **184**, 106452
10. Carew, J. S., and Huang, P. (2002) Mitochondrial defects in cancer. *Mol. Cancer* **1**, 9
11. Zhu, Z., Chen, D., Zhang, W., Zhao, J., Zhi, L., Huang, F., *et al.* (2018) Modulation of alternative splicing induced by paclitaxel in human lung cancer. *Cell. Death. Dis.* **9**, 491

12. Penjweini, R., Roarke, B., Alspaugh, G., Gevorgyan, A., Andreoni, A., Pasut, A., *et al.* (2020) Single cell-based fluorescence lifetime imaging of intracellular oxygenation and metabolism. *Redox. Biol.* **34**, 101549
13. Huang, L., Yu, Z., Zhang, T., Zhao, X., and Huang, G. (2014) HSP40 interacts with pyruvate kinase M2 and regulates glycolysis and cell proliferation in tumor cells. *PLoS One* **9**, e92949
14. Chandel, N. S., and Schumacker, P. T. (1999) Cells depleted of mitochondrial DNA (rho0) yield insight into physiological mechanisms. *FEBS Lett.* **454**, 173–176
15. Penjweini, R., Andreoni, A., Rosales, T., Kim, J., Brenner, M. D., Sackett, D. L., *et al.* (2018) Intracellular oxygen mapping using a myoglobin-mCherry probe with fluorescence lifetime imaging. *J. Biomed. Opt.* **23**, 1–14
16. Sedlack, A. J. H., Penjweini, R., Link, K. A., Brown, A., Kim, J., Park, S. J., *et al.* (2022) Computational modeling and imaging of the intracellular oxygen gradient. *Int. J. Mol. Sci.* **23**, 12597
17. Valente, A. J., Maddalena, L. A., Robb, E. L., Moradi, F., and Stuart, J. A. (2017) A simple ImageJ macro tool for analyzing mitochondrial network morphology in mammalian cell culture. *Acta. Histochem.* **119**, 315–326
18. Merrill, R. A., Flippo, K. H., and Strack, S. (2017) Measuring mitochondrial shape with ImageJ. In: Strack, S., Usachev, Y. M., eds. *Techniques to Investigate Mitochondrial Function in Neurons*, Springer, New York, NY: 31–48. New York
19. Hebert, B., Costantino, S., and Wiseman, P. W. (2005) Spatiotemporal image correlation spectroscopy (STICS) theory, verification, and application to protein velocity mapping in living CHO cells. *Biophys. J.* **88**, 3601–3614
20. Wiseman, P. W. (2013) Image correlation spectroscopy: mapping correlations in space, time, and reciprocal space. *Methods. Enzymol.* **518**, 245–267
21. Joubert, F., and Puff, N. (2021) Mitochondrial cristae architecture and functions: lessons from minimal model. *Syst. Membranes (Basel)* **11**, 465
22. Jonckheere, A. I., Smeitink, J. A., and Rodenburg, R. J. (2012) Mitochondrial ATP synthase: architecture, function and pathology. *J. Inherit. Metab. Dis.* **35**, 211–225
23. Ramanathan, B., Jan, K.-Y., Chen, C.-H., Hour, T.-C., Yu, H.-J., and Pu, Y.-S. (2005) Resistance to paclitaxel is proportional to cellular total antioxidant capacity. *Cancer. Res.* **65**, 8455–8460
24. Faridi, U., Alatawi, F., and Mostafa, M. (2017) Protective role of tocopherol and ascorbic acid in taxol-treated human erythrocytes in vitro. *Toxicol. Res. Appl.* **1**, 2397847317705813
25. Mukherjee, K., Chio, T. I., Sackett, D. L., and Bane, S. L. (2015) Detection of oxidative stress-induced carbonylation in live mammalian cells. *Free. Radic. Biol. Med.* **84**, 11–21
26. Penjweini, R., Roarke, B., Alspaugh, G., Link, K. A., Andreoni, A., Mori, M. P., *et al.* (2022) Intracellular imaging of metmyoglobin and oxygen using new dual purpose probe EYFP-Myoglobin-mCherry. *J. Biophotonics* **15**, e202100166
27. Zorova, L. D., Popkov, V. A., Plotnikov, E. Y., Silachev, D. N., Pevzner, I. B., Jankauskas, S. S., *et al.* (2018) Mitochondrial membrane potential. *Anal. Biochem.* **552**, 50–59
28. Hoffmann, R. F., Jonker, M. R., Brandenburg, S. M., de Bruin, H. G., ten Hacken, N. H. T., van Oosterhout, A. J. M., *et al.* (2019) Mitochondrial dysfunction increases pro-inflammatory cytokine production and impairs repair and corticosteroid responsiveness in lung epithelium. *Sci. Rep.* **9**, 15047
29. Zhou, X., Li, R., Chen, R., and Liu, J. (2020) Altered mitochondrial dynamics, biogenesis, and functions in the paclitaxel-resistant lung adenocarcinoma cell line a549/taxol. *Med. Sci. Monit.* **26**, e918216
30. Fonseca, M., Morgan, J., Brooks, T., Lycan, T., Strowd, R., Cubillos-Ruiz, J., *et al.* (2021) Effects of paclitaxel in mitochondrial function and cellular phenotype in human peripheral blood mononuclear cells and monocytes. *J. Pain* **22**, 580
31. Chavez, J. D., Keller, A., Zhou, B., Tian, R., and Bruce, J. E. (2019) Cellular interactome dynamics during paclitaxel treatment. *Cell. Rep.* **29**, 2371–2383.e2375
32. Loiseau, D., Chevrollier, A., Douay, O., Vavasseur, F., Renier, G., Reynier, P., *et al.* (2002) Oxygen consumption and expression of the adenine nucleotide translocator in cells lacking mitochondrial DNA. *Exp. Cell. Res.* **278**, 12–18
33. Keeley, T. P., and Mann, G. E. (2019) Defining physiological normoxia for improved translation of cell physiology to animal models and humans. *Physiol. Rev.* **99**, 161–234
34. Marroquin, L. D., Hynes, J., Dykens, J. A., Jamieson, J. D., and Will, Y. (2007) Circumventing the crabtree effect: replacing media glucose with galactose increases susceptibility of HepG2 cells to mitochondrial toxicants. *Toxicol. Sci.* **97**, 539–547
35. Leung, E., Cairns, R. A., Chaudary, N., Vellanki, R. N., Kalliomaki, T., Moriyama, E. H., *et al.* (2017) Metabolic targeting of HIF-dependent glycolysis reduces lactate, increases oxygen consumption and enhances response to high-dose single-fraction radiotherapy in hypoxic solid tumors. *BMC. Cancer.* **17**, 418
36. Ranjit, S., Malacrida, L., Stakic, M., and Gratton, E. (2019) Determination of the metabolic index using the fluorescence lifetime of free and bound nicotinamide adenine dinucleotide using the phasor approach. *J. Biophotonics.* **12**, e201900156
37. Jiang, H., Qi, Y. T., Wu, W. T., Wen, M. Y., Liu, Y. L., and Huang, W. H. (2020) Intracellular monitoring of NADH release from mitochondria using a single functionalized nanowire electrode. *Chem. Sci.* **11**, 8771–8778
38. Cao, R., Wallrabe, H., Siller, K., Rehman Alam, S., and Periasamy, A. (2019) Single-cell redox states analyzed by fluorescence lifetime metrics and tryptophan FRET interaction with NAD(P)H. *Cytometry A* **95**, 110–121
39. Wallrabe, H., Svindrych, Z., Alam, S. R., Siller, K. H., Wang, T., Kashatus, D., *et al.* (2018) Segmented cell analyses to measure redox states of autofluorescent NAD(P)H, FAD & Trp in cancer cells by FLIM. *Sci. Rep.* **8**, 79
40. Chen, H., and Chan, D. C. (2009) Mitochondrial dynamics–fusion, fission, movement, and mitophagy–in neurodegenerative diseases. *Hum. Mol. Genet.* **18**, R169–R176
41. Boldogh, I. R., and Pon, L. A. (2007) Mitochondria on the move. *Trends. Cell. Biol.* **17**, 502–510
42. Chung, J. Y., Steen, J. A., and Schwarz, T. L. (2016) Phosphorylation-induced motor shedding is required at mitosis for proper distribution and passive inheritance of mitochondria. *Cell. Rep.* **16**, 2142–2155
43. Jordan, M. A., and Wilson, L. (2004) Microtubules as a target for anticancer drugs. *Nat. Rev. Cancer.* **4**, 253–265
44. Komlodi-Pasztor, E., Sackett, D., Wilkerson, J., and Fojo, T. (2011) Mitosis is not a key target of microtubule agents in patient tumors. *Nat. Rev. Clin. Oncol.* **8**, 244–250
45. Varbiro, G., Veres, B., Gallyas, F., Jr., and Sumegi, B. (2001) Direct effect of Taxol on free radical formation and mitochondrial permeability transition. *Free. Radic. Biol. Med.* **31**, 548–558
46. Wu, M., Kalyanasundaram, A., and Zhu, J. (2013) Structural and biomechanical basis of mitochondrial movement in eukaryotic cells. *Int. J. Nanomedicine.* **8**, 4033–4042
47. Ding, W. X., and Yin, X. M. (2012) Mitophagy: mechanisms, pathophysiological roles, and analysis. *Biol. Chem.* **393**, 547–564
48. Suen, D. F., Norris, K. L., and Youle, R. J. (2008) Mitochondrial dynamics and apoptosis. *Genes. Dev.* **22**, 1577–1590
49. Woods, L. C., Berbusse, G. W., and Naylor, K. (2016) Microtubules are essential for mitochondrial dynamics-fission, fusion, and motility-in Dictyostelium discoideum. *Front. Cell. Dev. Biol.* **4**, 19
50. Xu, Y., Xue, D., Bankhead, A., 3rd, and Neamati, N. (2020) Why all the fuss about oxidative phosphorylation (OXPHOS)? *J. Med. Chem.* **63**, 14276–14307
51. Peng, J., Cui, Y., Xu, S., Wu, X., Huang, Y., Zhou, W., *et al.* (2021) Altered glycolysis results in drug-resistant in clinical tumor therapy. *Oncol. Lett.* **21**, 369
52. Tomlinson, M. J., Tomlinson, S., Yang, X. B., and Kirkham, J. (2013) Cell separation: terminology and practical considerations. *J. Tissue. Eng.* **4**, 2041731412472690
53. Dave, Z., Byfield, M., and Bossy-Wetzel, E. (2008) Assessing mitochondrial outer membrane permeabilization during apoptosis. *Methods* **46**, 319–323

54. Bolte, S., and CordeliÈRes, F. P. (2006) A guided tour into subcellular colocalization analysis in light microscopy. *J. Microsc.* **224**, 213–232
55. Gottlieb, E., Armour, S. M., Harris, M. H., and Thompson, C. B. (2003) Mitochondrial membrane potential regulates matrix configuration and cytochrome c release during apoptosis. *Cell Death Differ.* **10**, 709–717
56. Barrientos, A., and Moraes, C. T. (1999) Titrating the Effects of Mitochondrial Complex I Impairment in the Cell Physiology. *J. Biol. Chem.* **274**, 16188–16197
57. Kenwood, B. M., Weaver, J. L., Bajwa, A., Poon, I. K., Byrne, F. L., Murrow, B. A., *et al.* (2014) Identification of a novel mitochondrial uncoupler that does not depolarize the plasma membrane. *Mol. Metab.* **3**, 114–123
58. Alspaugh, G., Roarke, B., Chand, A., Penjweini, R., Andreoni, A., and Knutson, J. R. (2021) Developing analysis protocols for monitoring intracellular oxygenation using fluorescence lifetime imaging of myoglobin-mCherry. *Methods Mol. Biol.* **2304**, 315–337